Retrieval of Cirrus Cloud Radiative and Backscattering Properties Using Combined Lidar and Infrared Radiometer (LIRAD) Measurements

JENNIFER M. COMSTOCK* AND KENNETH SASSEN

Department of Meteorology, University of Utah, Salt Lake City, Utah

(Manuscript received 28 August 2000, in final form 11 April 2001)

ABSTRACT

A method for retrieval of cirrus macrophysical and radiative properties using combined ruby lidar and infrared radiometer measurements is explained in detail. The retrieval algorithm includes estimation of a variable backscatter-to-extinction ratio for each lidar profile, which accounts for changes in cloud microphysical properties with time. The technique also utilizes a correlated *K* distribution radiative transfer model, where absorption coefficients *K* have been tabulated specifically for the bandwidth and filter function of the infrared radiometer. The radiative transfer model allows for estimation of infrared emission due to atmospheric water vapor, ozone, and carbon dioxide, which is essential for deriving cirrus radiative properties. Also described is an improved technique for estimation of upwelling IR radiation that is emitted by the surface of the earth and reflected by the cloud into the radiometer field of view. Derived cirrus cloud properties include base and top height and temperature, visible optical depth, emittance, backscatter-to-extinction ratio, and extinction-to-absorption ratio. The purpose of this algorithm is to facilitate the analysis of the extensive high-cloud dataset obtained at the University of Utah's Facility for Atmospheric Remote Sensing in Salt Lake City, Utah. To illustrate the method, a cirrus case study is presented.

1. Introduction

Due to the uncertainty of the effects of cirrus clouds on the earth's radiation budget and feedback to atmospheric dynamics (Liou 1986), there has been an increased interest in the retrieval of cirrus macrophysical, microphysical, and radiative properties using both passive and active remote sensing techniques (Platt 1973; Ou et al. 1993; Smith et al. 1993; Matrosov et al. 1994). Knowledge of cirrus cloud properties and their inherent inhomogeneity will help to improve their representation in cloud models of all scales (e.g., cloud resolving, single column, and global climate models). Satellite retrieval algorithms also rely on knowledge of cloud radiative properties, therefore, improved measurements from surface-based instruments will enhance satellite cloud detection and analysis schemes.

Macrophysical properties obtained in this study include lidar-derived cloud base and top height, as well as cloud temperature inferred from radiosonde measurements. By combining lidar and infrared (IR) radiometric measurements, both visible optical depth τ and cloud emittance ε can be obtained. This combined remote sensor technique is commonly known as the LIRAD method and is described in Platt and Dilley (1981). In this paper, we will briefly outline the original LIRAD method, as well as the variations that we have made in the present algorithm. These modifications include a method for estimating the backscatter-to-extinction ratio for each lidar profile, rather than a single value for the entire observation period. Also described is a new technique for determining the amount of IR radiance that is emitted by the earth and reflected by the cloud into the radiometer field of view (FOV). Our results show that this value can be significant, particularly if the ice crystals in the cloud are relatively small.

A description of the instrumentation used in this study will be presented in section 2, followed by a review of the original LIRAD technique in section 3a. Our new retrieval of visible optical depth is presented in section 3b, which includes estimation of cloud boundaries, backscatter-to-extinction ratio k, and multiple-scattering parameter η. In section 4, the radiative transfer model used to estimate cloudless-sky downwelling radiance in the atmospheric window is presented, which is important in the calculation of ε. The retrieval of cloud radiative properties is detailed in section 5, including determination of the upwelling IR radiance that is reflected by the cloud into the IR radiometer FOV, which must

* Current affiliation: Pacific Northwest National Laboratory (PNNL), Richland, Washington. PNNL is operated by Battelle Corporation for the U.S. Department of Energy.

Corresponding author address: Jennifer Comstock, Pacific Northwest National Laboratory, P.O. Box 999, MSIN K9-24, Richland, WA 99352.
E-mail: jennifer.comstock@pnl.gov

TABLE 1. FARS instrumentation used in the LIRAD-radiation method.

Instrument list
Polarization cloud lidar
Two channels
Vertical polarization transmitted
Manually "tiltable" ±5° from zenith
0.1-Hz PRF, 7.5-m maximum range resolution
Maximum 2 K per channel data record length
1–3 mrad receiver beamwidths
25-cm diameter telescope
0.694-μm wavelength, 1.5-J maximum output
8-bit digitizer board
IR radiometer
Narrow beam (0.14° FOV)
9.5–11.5 μm bandwidth
Microwave radiometer
Two frequencies (23.8 and 31.4 GHz)

be modeled for the ε calculations. A detailed sensitivity analysis is in section 6, followed by a case study demonstrating the abilities of the retrieval algorithm (section 7) and conclusions (section 8).

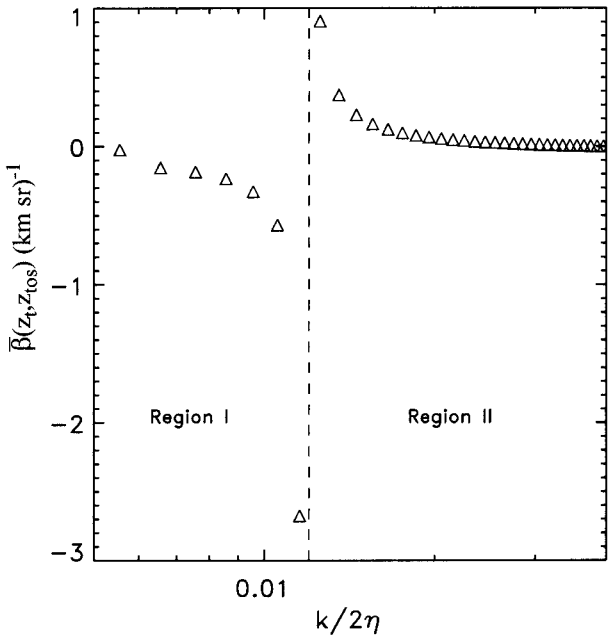

FIG. 1. Average β_c between cloud top and the lidar signal maximum height estimated using various values of $k/2\eta$. Region I denotes the unstable solution, while region II denotes the stable solution, to Eqs. (12) and (13).

2. Instrumentation

In support of the First ISCCP (International Satellite Cloud Climatology Program) Regional Experiment (FIRE; Cox et al. 1987), ground-based remote sensing observations of high clouds have been recorded at the Facility for Atmospheric Remote Sensing (FARS) in Salt Lake City, Utah, since 1986. FARS is located at 40°46′00″N, 111°49′38″W at an elevation of 1.52 km above mean sea level. A complete list of FARS instrumentation and history is described in Sassen et al. (2001a).

The lidar system used in this study is a vertically pointing dual-polarization ruby lidar that operates at 0.1 Hz with a maximum vertical resolution of 7.5 m. Table 1 provides a complete list of instrument specifications for the ruby lidar, as well as the other instruments used in this study. Lidar calibrations are performed by positioning a randomly polarized light source at the minimum telescope focus distance (Sassen et al. 2001a). In order to ensure data quality, each lidar signal is examined using an algorithm that detects errors in both the background and the recorded backscattered energy (Barnett 2000). By inspecting the background signal, noisy background signals, offscale background settings, and pretrigger errors are identified. Errors identified by inspecting the recorded backscattered energy include instances when the oscilloscope falsely triggers, as well as when no data are recorded. The laser output power and photomultiplier tube voltage are also checked for proper values. In the event that an error is detected, the profile is not included in the data analysis.

The radiometer is a midinfrared Precision Radiation Thermometer (model PRT-5) that has been modified to have a narrow FOV. The PRT-5 is manufactured by the Pyrometer Instrument Company, Inc. and has a bandwidth that lies within the atmospheric window. The PRT-5 is designed to measure the vertical downwelling radiance emitted from water, ice, aerosols, clear-sky molecular background, and other substances that fill its FOV. The IR radiometer is coaligned with the ruby lidar so that both instruments are simultaneously sampling the same portion of the cloud. The radiometer has been calibrated by the manufacturer approximately once every two years, and comparisons with both spectral instruments and model-derived radiances ensure proper performance between calibrations (Barnett 2000).

Recently, FARS has acquired a model WVR-1100 dual-frequency radiometer manufactured by Radiometrics Corporation that measures microwave radiation emitted from the atmosphere at 23.8 GHz (K band) and 31.4 GHz (Ka band). The microwave radiometer (MWR) is used to derive column-integrated liquid water and water vapor from measurements of atmospheric brightness temperature. The 31.4-GHz channel mainly records microwave emission from cloud liquid while the 23.8-GHz channel is dominated by microwave emission from water vapor, allowing a simultaneous but separate retrieval of path-integrated liquid and vapor from the measured radiances. In this study, only the water vapor channel is used because cirrus clouds are primarily dominated by ice, and in the event that supercooled liquid water droplets are present, the emitted microwave energy is well below the detection threshold of the instrument (~2.73 K). MWR mea-

surements are used to correct variations in the column water vapor between radiosonde profiles to more accurately represent the actual water vapor mixing ratios, which are needed in the calculation of cloud IR emittance.

Radiosonde measurements are obtained from the Salt Lake City National Weather Service Forecast Office (SLC-NWSFO) and are available twice daily at 0000 and 1200 UTC. Prior to June 1998, the SLC-NWSFO used the Viz B-2 sonde, but more recently switched to the Vaisala radiosonde, which is equipped with the RS-80 H-humicap sensor. Recent studies have demonstrated that Vaisala sensors are approximately 10%–15% drier than water vapor profiles derived from Raman lidar measurements during the daytime, and 5% drier during the nighttime (Turner et al. 2000). Scaling radiosonde-derived water vapor profiles using MWR measurements can improve the daytime radiosonde dewpoint measurements to within 5% of the Raman lidar–derived values (Turner et al. 1998).

3. Methodology

The next section presents a brief account of the original LIRAD method, pioneered by C. M. R. Platt, followed by a detailed description of the current methodology used to estimate cirrus radiative and backscattering properties. The LIRAD method as described in Platt and Dilley (1981) is repeated for historical purposes and to provide the background needed to understand changes made to it in the present study. (A list of symbols is given in the appendix.)

a. Original LIRAD technique

The in-cloud attenuated isotropic backscatter coefficient $B'_c(\pi, z)$ (km^{-1}) is measured directly by the lidar receiver and is related to the actual isotropic backscatter coefficient $B_c(\pi, z)$ by the equation

$$B_c(\pi, z) = B'_c(\pi, z)\left[1 - \left(\frac{2\eta}{k}\right)\int_{z_b}^{z} B'_c(\pi, z'')\, dz''\right]^{-1}, \quad (1)$$

where z_b is cloud-base height. According to Platt and Dilley (1981), $B_c(\pi, z)$ is equal to 4π times the actual backscatter coefficient. The parameter $B_c(\pi, z)$ and the volume extinction coefficient σ_c (km^{-1}) at the lidar wavelength are related through the backscatter-to-extinction ratio k, where

$$k = \frac{B_c(\pi, z)}{\sigma_c(z)}. \quad (2)$$

The parameters k and η, which accounts for multiple scatter, are assumed to be independent of height. The IR volume absorption coefficient σ_a (km^{-1}) is related to $B_c(\pi, z)$ through the equation

$$\sigma_a(z) = \left(\frac{1}{2\eta\alpha}\right)\left(\frac{2\eta}{k}\right)B_c(\pi, z), \quad (3)$$

where α is defined as

$$\alpha = \frac{\sigma_c(z)}{\sigma_a(z)}, \quad (4)$$

and, like k, is assumed to be independent of z. The integrated backscatter $\gamma'(\pi)$ is defined as

$$\gamma'(\pi) = \int_{z_b}^{z_t} B'_c(\pi, z)\, dz, \quad (5)$$

where z_t is cloud-top height.

Cloud emittance is calculated using the following process. An initial guess of the parameter $k/2\eta$ is inserted into Eq. (1) and $B_c(\pi, z)$ is calculated at each level of the atmosphere. Using an initial guess of the quantity $2\eta\alpha$, the IR absorption coefficient is estimated via Eq. (3). A theoretical cloud radiance I_{ct} is calculated using the equation

$$I_{ct} = \int_{z_o}^{z_t} \sigma_a(z) I_b(z) \exp\left[-\int_{z_o}^{z} \sigma_a(z'')\, dz''\right] dz + I_{\text{sc}}. \quad (6)$$

The first term in Eq. (6) represents emission by cloud particles and I_{sc} corrects for in-cloud emitted radiance that is scattered into the radiometer FOV. The blackbody radiance I_b is calculated at the IR radiometer wavelength using radiosonde-derived temperature. The measured cloud radiance I_c is derived from the IR radiometer measurement by subtracting out emission I_{sky} due to atmospheric gases below cloud according to

$$I_c = \frac{I_m - I_{\text{sky}}}{T_{\text{bc}}}, \quad (7)$$

where I_{sky} and the transmittance T_{bc} below the cloud are estimated using a radiative transfer model. The values of the theoretical and measured cloud radiances are then compared to one another. If I_{ct} and I_c are different by more than 1%, a new value of $2\eta\alpha$ is inserted into Eq. (3) and the calculation of σ_a is repeated until I_{ct} and I_c are within 1%. Once a final value of $\sigma_a(z)$ is determined the cloud emittance can be calculated using

$$\varepsilon = 1 - \exp\left[-\int_{z_b}^{z_t} \sigma_a(z)\, dz\right]. \quad (8)$$

This process is repeated for each lidar profile observed in a single observation period.

Once ε and $\gamma'(\pi)$ are determined for each lidar profile, a curve of the form

$$\gamma'(\pi) = \frac{k}{2\eta}\left\{1 - \exp\left[-2\eta\alpha \ln\left(\frac{1}{1 - \varepsilon}\right)\right]\right\} \quad (9)$$

is fit to the results by numerically solving for the coefficients $2\eta\alpha$ and $k/2\eta$. It can be shown that when ε

$\rightarrow 1$, $\gamma'(\pi) = k/2\eta$. The final value of $k/2\eta$ is the mean value for the entire cloud system. If this numerically derived value of $k/2\eta$ is different from the initial value used in Eq. (1), the entire process starting with Eq. (1) is repeated with the new value of $k/2\eta$. All of the above calculations are repeated until a consistent value for $k/2\eta$ is found between iterations. According to Platt and Dilley (1981), this iterative method produces emittance with an accuracy of approximately $\pm 10\%$.

b. Lidar signal processing and determination of visible optical depth

The following sections describe the new approach that is used in this study to determine cloud backscattering properties and visible optical depth.

1) Lidar backscattered energy and depolarization ratio

The ruby lidar backscattered power P as a function of range R measured by the receiver is described by the single-scattering lidar equation

$$P(R) = \frac{C}{R^2}[\beta(R) + \beta'(R)] \times \exp\left[-2\int_0^R \eta(R)\sigma(R)\, dR\right], \quad (10)$$

where C is the lidar system constant, σ is the extinction coefficient, and $\eta(R)$ is the range-dependent forward multiple-scattering correction parameter. The parameters β and β' represent the backscatter coefficient for single- and multiple-scattered photons, respectively. Power $P(R)$ is measured for both the parallel ($\parallel$) and perpendicular ($\perp$) planes of polarization with respect to the incident polarization plane.

The linear depolarization ratio δ is defined as the ratio of the perpendicular to the parallel polarized lidar signals and is expressed as

$$\delta = \frac{P_\perp(R)}{P_\parallel(R)}, \quad (11)$$

which can be used to distinguish cloud phase and detect the orientation of certain types of ice crystals. Sassen (1991) provides an overview of different scatterers and their corresponding δ values. For example, spherical water droplets produce virtually no depolarization ($\delta \sim 0.0$), ice crystals and snowflakes can produce $\delta \sim 0.5$, and rimed ice and particles with complex surfaces have $\delta > 0.6$. Platt (1978) and Sassen and Benson (2001) have demonstrated that horizontally oriented hexagonal plate crystals produce depolarization values less than 0.15.

2) Estimation of cloud boundaries

Due to attenuation of lidar signals as cloud optical depths increase above $\tau \sim 3$ (Kinne et al. 1992; Sassen 2001), cloud-top heights of dense clouds become difficult to detect. This can also result from the limited dynamic range of lidar detectors, where weak signals are often lost when channel gains are reduced to accommodate cloud regions containing strong signals, especially from horizontally oriented plate crystals. Cloud radars, such as the FARS 3.2-mm (95 GHz) radar (Sassen et al. 2001a), are capable of penetrating through dense clouds; however, they are unable to detect small ice crystals due to their longer transmitting wavelength. Continuous radar measurements do not coincide with the ruby lidar dataset; therefore, only lidar is used to identify cloud boundaries.

Cloud heights are determined by first identifying the region where the cloud exists by inspecting height versus time displays of lidar backscattered energy measured for each observation period. For example, if the actual cloud base and top are 8 and 10 km, respectively, a window of 7.5 and 10.5 km would be chosen for the cloud height detection algorithm. Creating a window where only cirrus is located eliminates contamination of the dataset from lower water clouds or aerosol layers. A numerical algorithm then locates the actual cloud base using a running average of three consecutive points of the height normalized lidar signal, starting below cloud. The largest signal increase is determined by taking a ratio of the unaveraged signal to the average signal (Sassen and Cho 1992). If this ratio is greater than 1.3 (in our case), then z_b is defined as the point where the largest signal increase occurs for the three points used in the average signal. Cloud-top height z_t is determined using a reference cloud-free signal derived from Rayleigh scattering theory for molecules following Young (1995).

3) Cloud backscatter coefficient

In the present retrieval technique, the cloud backscatter coefficient β_c (km sr)$^{-1}$ is determined using a slightly different equation than is used in the original LIRAD method. The total backscatter coefficient measured by the lidar includes both cloud and molecular scattering. The parameter β_c is calculated using (Fernald et al. 1972; Sassen and Cho 1992)

$$\beta_c(z) = \frac{G(z_o, z)}{1 - \dfrac{2\eta}{k}\displaystyle\int_{z_o}^{z} G(z_o, z')\, dz'} - \beta_m(z) \quad (12)$$

and

$$G(z_o, z) = \beta_m(z_o)\frac{S(z)z^2}{S(z_o)z_o^2} \times \exp\left[2\left(\frac{8\pi}{3} - \frac{\eta}{k}\right)\int_{z_o}^{z} \beta_m(z'')\, dz''\right], \quad (13)$$

where the scattering contribution β_m from air molecules in the atmosphere is subtracted from the total backscatter coefficient and z_o denotes the height just below cloud base where the scattering is presumably due to molecules only and corresponds to the lidar signal minima $S(z_o)z_o^2$. Equations (12) and (13) are based on the ''clear-air'' scattering assumption where the boundary condition is provided by Rayleigh-scattering predictions for a pure molecular atmosphere. There are few aerosols present in the upper troposphere where most cirrus clouds reside, and the molecular-scattering boundary condition will hold true for most cirrus cases. Note that we have changed the symbol for cloud backscatter coefficient to help separate the two different methods.

By integrating $\beta_c(z)$ in Eq. (12) between z_b and z_t, cloud visible optical depth τ can be determined following

$$\tau = \frac{1}{k}\int_{z_b}^{z_t} \beta_c(z)\, dz. \tag{14}$$

4) BACKSCATTER-TO-EXTINCTION RATIO k

The backscatter-to-extinction ratio k (sr^{-1}) is equivalent to the normalized scattering phase function $\mathcal{P}$ with scattering angle Θ at 180°, or $\mathcal{P}(\pi)/4\pi$, and is a measure of the backward strength of cloud particle scattering. The definition of k used in this study is slightly different from that used in the original LIRAD studies, where k is 4π times the normalized scattering phase function and is unitless.

The backscatter phase function primarily depends on ice crystal shape, as shown in Takano and Liou (1995). Sassen (1978) reports laboratory and field derived values of k obtained with a 0.6328-μm wavelength laser for various ice crystal types, concluding that k appears to vary with ice crystal habit and orientation. The results of both Sassen (1978) and Takano and Liou (1995) indicate that simple ice crystals, such as hollow columns, tend to have lower values of $\mathcal{P}(\pi)$ when compared with more complex crystals, such as aggregates and bullet rosettes.

Due to the inherent inhomogeneity of cirrus clouds, k will vary as the cloud evolves and ice crystal habits change. The present study determines k by first calculating the average backscatter coefficient above cloud top, expressed as $\overline{\beta}(z_t, z_{\text{tos}})$ for various values of the combined scattering parameter $k/2\eta$ corresponding to a k of 0.01 and 0.2 sr^{-1}. The parameter z_{tos} denotes the maximum height recorded by the lidar and $\overline{\beta}(z_t, z_{\text{tos}})$ represents the average molecular backscatter above cloud. Graphing $\overline{\beta}(z_t, z_{\text{tos}})$ versus $k/2\eta$ (Fig. 1), the appropriate value of $k/2\eta$ falls in the region where the change in slope approaches zero (i.e., region II in Fig. 1). This approach for selecting $k/2\eta$ minimizes the chance that $k/2\eta$ will cause an unstable or negative solution for β_c (region I in Fig. 1) between cloud base and top, which can occur if $k/2\eta$ is underestimated. The parameter k is subsequently determined from an estimate of η, which is described in the following subsection.

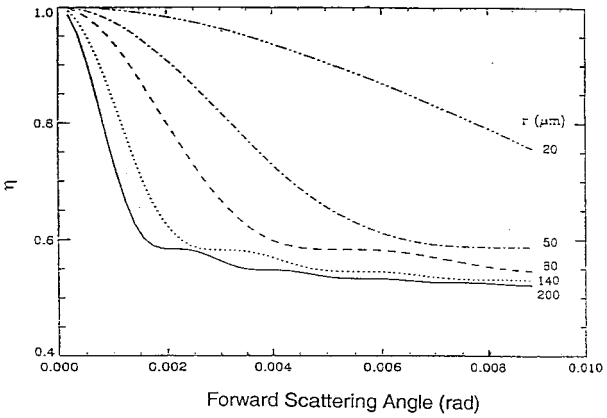

FIG. 2. Multiple-scattering parameter η as a function of forward-scattering angle (or FOV) and mean effective radius r_e for spherical ice particles.

The maximum value of k was chosen based on the effect of horizontally oriented plate crystals on the lidar backscattered signal. Platt (1978) revealed that a maximum value of $k = 800$ occurs when there are a large number of precisely horizontally oriented plate crystals in the scattering medium. Ice crystals never fall with exactly 0° of wobble, but rather with a slight tilt from the horizontal (Sassen 1991). In this situation, δ will be low and the backscattered energy will be strong. Therefore, we have limited the maximum k derived from lidar observations of cirrus clouds to about 0.2, which corresponds to a tilt of approximately 10° off the horizontal (Platt 1978). The minimum value of $k = 0.01$ was chosen to help analyze weak signals that can occur in thin and subvisual cirrus clouds.

5) MULTIPLE-SCATTERING PARAMETER η

The amount of multiple-scattered returns of a laser pulse that occurs in a cirrus cloud depends on the width of the diffraction peak in the phase function. Forward multiple-scattering contribution to lidar returns are also dependent on the angular FOV of the lidar receiver, cloud range, and cloud depth. Scattering phase functions for nonspherical ice crystals are highly forward peaked (Takano and Liou 1995), particularly at visible wavelengths. It is generally assumed that photons returning to the lidar receiver have undergone one large angle (~180°) scattering event, which may be preceded and/or followed by multiple forward-scattering events. Nicolas et al. (1997) demonstrate that lidar signals penetrating cirrus clouds with optical depths less than 1.0 will be dominated by single or double scatterings, while multiple scattering will dominate for optical depths greater than 1.0, implying that exact shape of $\mathcal{P}(\Theta)$

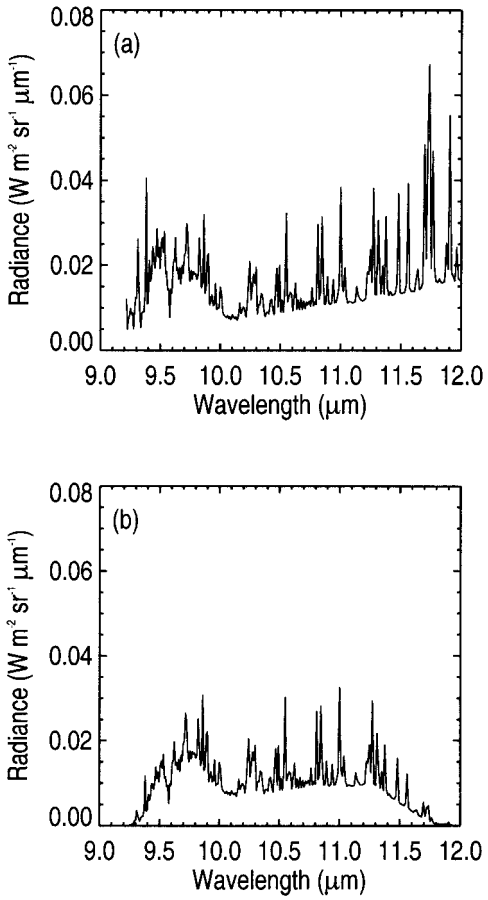

FIG. 3. Model downwelling radiance calculated by MODTRAN3 for (a) nonfiltered radiance and (b) with the PRT-5 radiometer filter function applied.

around 180° will not be a major determinant of the received signal.

The parameter that has been historically used to account for error in the single-scattering lidar equation due to multiple scattering is the parameter η (Platt 1973). Multiple-scattering corrections are required in the exponential attenuation term of Eq. (10). The parameter $\eta(R)$ accounts for the multiple scattering as a result of captive diffraction. Due to the forward peak in cirrus ice crystal phase functions, scattering of the lidar pulse will be dominated by forward scattering, and thus some diffracted photons will remain indefinitely in the laser beam. The factor $\eta(R)$ corrects the single-scattering lidar equation for the apparent decrease in the extinction rate, which causes an underestimation of cloud optical depth. However, $\eta(R)$ does not correct for multiple scattering that includes a primary backscattering event. The parameter β' in Eq. (10) does correct for this type of multiple scattering. There is no solution currently available describing β', so we have neglected it rather than include it in the exponential attenuation term.

Platt (1981) shows that η generally increases in the first 1–2 km of the cloud, but then levels off as cloud penetration increases beyond that point. However, there is little information available that can help to correct for the variation of η with height. Therefore, in the present study, we assume that η is independent of height when analyzing lidar signal returns.

Values of η used in previous studies vary widely. Platt (1973) extracted a value of $\eta = 0.41 \pm 0.15$ from cirrus observations, while Sassen and Cho (1992) used a value of 0.75 in their evaluation of optically thin clouds. Monte Carlo simulations of η performed by Platt (1981) produced values between 0.0 and 0.6, depending on the scattering phase function and cloud penetration depth. Platt et al. (1998) have subsequently developed a linear relationship between η and midcloud temperature. In this study, η ranges between 0.6 and 0.9. These values were derived from Mie calculations of forward multiple scattering using a similar method as described in Sassen and Zhao (1995). Figure 2 depicts the variation of η with FOV and effective radius of spherical ice particles. The forward diffraction peak of ice crystal phase functions increases as the size becomes larger for a constant wavelength. This is true for both spherical and hexagonal ice crystal shapes. The forward diffraction peak will not change significantly with ice crystal shape, as shown by theoretical simulations of phase functions reported in Macke et al. (1996). The ruby lidar was typically operated with a 1.0-mrad receiver FOV, but occasionally at 3.0 mrad. As Fig. 2 illustrates, at 1 mrad η will have a value ranging from approximately 0.7 to 0.98 depending on the particle radius. For a FOV of 3 mrad, the range is 0.6–0.95. Similar values are also reported by Eloranta (1998) using an analytical model that estimates multiply scattered lidar returns. Typically, using an $\eta < 0.5$ will result in unrealistically high values of τ, beyond the limit of the measurement capabilities of backscatter lidars using analog detectors, which occurs at $\tau \sim 3$.

In the present method, the appropriate value of η is chosen for each data period based on cloud observations reported in field notes and by examining height versus time displays of lidar backscatter returns. Each observing period was divided into sections based on apparent homogeneity. For example, a cloud system may begin as an optically and physically thin cloud, in which case a value of $\eta = 0.9$ was used because the scattering is dominated by single backscattering (with some forward scattering). As the cloud thickens, multiple scattering becomes more important, and $\eta = 0.8$ is used. If the cloud develops to the point where the lidar signal becomes attenuation limited ($\tau \rightarrow 3$), scattering will be dominated by multiple scattering, and therefore an η of 0.6 is used. The minimum and maximum values of η used are 0.6 and 0.9.

c. Radiative transfer model for the estimation of clear-sky radiance

The IR radiometer measurement includes emission from all absorbing gases, aerosols, and cloud particles

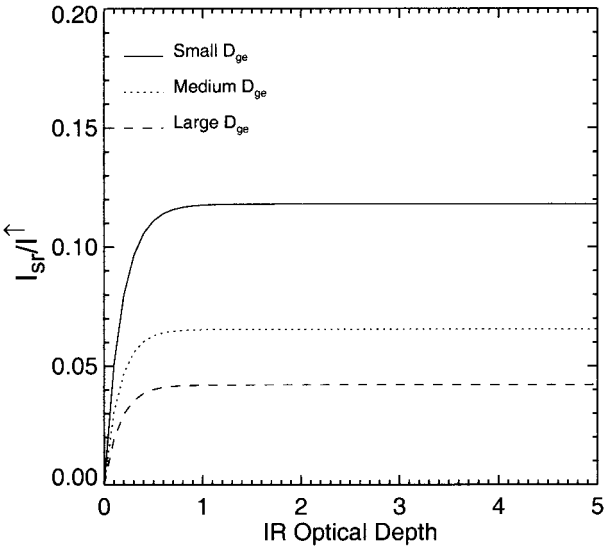

FIG. 4. Fraction of upwelling radiance that is reflected off the cloud into radiometer FOV derived from model simulations. The different curves denote changes in scattered radiance due to generalized effective size D_{ge}.

in the FOV of the instrument. In the LIRAD method, the radiometer measurement is used to retrieve the emission from cloud particles only, which is needed to calculate cloud emittance ε. Hence, contributions from atmospheric gases and aerosols must be removed from the total downwelling radiance measurement. The amount of radiance emitted by atmospheric constituents can be estimated with a radiative transfer model, which is described in the following subsections. Aerosol absorption is generally assumed to be negligible; however, in cases where the lidar detected a dense aerosol layer, the case was either avoided or a temporally near-cloudless sky background IR radiometer measurement was used to obtain the cloud radiance. Generally, aerosols will not affect the measured IR radiance unless the aerosol is highly absorbing, such as carbon. Aerosols will influence the scattering of visible wavelength radiation; however, this will not affect the retrieval in this study.

1) CORRELATED *K* DISTRIBUTION METHOD

The thermal infrared window between 9.0 and 12.5 μm is a region of continuous absorption primarily due to water vapor (see Fig. 3a). However, strong absorption due to ozone O_3 exists at 9.6 μm, as well as weak absorption by carbon dioxide CO_2 at 10.6 μm. The primary contributor to the downwelling IR radiance (for the IR radiometer bandwidth) at the surface is water vapor, which contributes about 88% of the total downwelling clear-sky radiance (using radiances calculated from Salt Lake City, Utah, soundings for a 1-yr period). Other gases, such as O_3 and CO_2 contribute approximately 9% and 3%, respectively. Therefore, these atmospheric gases are included in the estimate of IR radiance. A computationally efficient method for calculating absorption coefficients K for inhomogeneous atmospheres is the correlated K distribution (CKD) method (Lacis et al. 1991). Note that we use an uppercase K to represent absorption coefficient, whereas k denotes the backscatter-to-extinction ratio.

The FARS CKD model used in the present study was developed by Duffy (1996), following the method described in Fu and Liou (1992). Absorption coefficients were calculated using the HITRAN database and the Fast Atmospheric Signature Code 3 (FASCOD3) developed by the Air Force Geophysics Laboratory (Clough et al. 1986). Duffy (1996) tabulated absorption coefficients at a resolution of 0.0004 cm^{-1} for four temperatures (180, 220, 260, and 300 K) and 20 pressures between 12.6 and 1000 mbar for each absorbing species. There are 119 cumulative probability functions $g(K)$ used in calculations of atmospheric transmittance.

The water vapor continuum is an important contributor to the downwelling radiance measured at the surface, but unfortunately there is still considerable uncertainty in representing continuum absorption in radiative transfer models. The continuum is attributed to the accumulation of absorption in the far wings of H_2O lines, which results from self-broadening and foreign collision broadening. It has also been suggested that the water vapor dimer $(H_2O)_2$ may contribute to continuum absorption (Clough et al. 1989). The FARS CKD model uses a parameterization that estimates the continuum absorption as a function of wavelength, temperature, pressure, and partial pressure of water vapor following Roberts et al. (1976).

2) TRANSMITTANCE AND RADIANCE CALCULATIONS

The transmittance $T_{\bar{\nu}}$ of each absorbing gas in each atmospheric layer is calculated directly from the cumulative probability functions using

$$T_{\bar{\nu}} = \int_0^1 \exp\left[-\int_{z_1}^{z_2} K(g, p, T)\rho \, dz\right] dg, \qquad (15)$$

where the mean layer density, pressure, and temperature (i.e., ρ, p, and T, respectively) are obtained from an atmospheric sounding profile. Since radiosonde measurements generally do not extend to 30 km, standard atmosphere data are added above the height where the measured profile ends. The vertical integration of the transmittance functions in g space and calculation of the total combined transmittance is obtained by assuming that the absorption coefficients of each gas are uncorrelated, which allows the transmittance for each gas to be multiplied together (Fu and Liou 1992).

Downwelling radiance at each level is estimated from the total transmittance using a radiative transfer equation expressed in z coordinates:

$$I_{\bar{\nu}}^{\downarrow}(z) = I_b(z_{\mathrm{TOA}})T_{\bar{\nu}}(z_{\mathrm{TOA}} - z) - \int_z^{z_{\mathrm{TOA}}} I_b(z')\left[\frac{d}{dz}T_{\bar{\nu}}(z' - z)\right] dz'. \quad (16)$$

The downwelling IR radiance at the top of the atmosphere is assumed to be negligible hence the first term in Eq. (16) is neglected. The blackbody radiance I_b is calculated using the mean layer temperature in the Planck function at an effective emission wavenumber for each absorbing gas. The effective wavenumber is estimated by first calculating the monochromatic radiance over the 833–1081 cm^{-1} bandwidth and then performing a spectral integration to obtain a total radiance over the spectral region. A second integration is performed over the spectral region to find the wavenumber that corresponds to half the total radiance. This process is repeated for a range of temperatures typical in the atmosphere. The effective wavenumber is then chosen to give the most accurate result for a wide variety of atmospheric conditions when comparing with a line-by-line model. Errors associated with assuming an effective wavenumber for Planck function calculations are less than 1% for tropical and midlatitude summer standard atmospheric profiles. Further detail concerning estimation of the effective wavenumber is described in Duffy (1996).

3) IR RADIOMETER FILTER FUNCTION

A PRT-5 type radiometer has a distinct filter function that reduces the actual measured radiance at various wavelengths. It is difficult to apply a filter function when using the CKD method because the wavelength dependence has been removed. To account for the reduction in the measured radiance, MODTRAN3 (Berk et al. 1989) was used to calculate the downwelling radiance at 1-μm intervals over the IR radiometer bandwidth, as displayed in Fig. 3a for a U.S. standard atmosphere. The filter function is applied to the MODTRAN3 results by multiplying the wavelength-dependent radiance $I(\lambda, z)$ by the filter function $\Phi(\lambda)$ as demonstrated in Fig. 3b. The filtered downwelling radiance across the PRT-5 bandpass is subsequently obtained by the integration

$$I^{\downarrow}(z) = \int_{\lambda_1}^{\lambda_2} \Phi(\lambda)I(\lambda, z)\, d\lambda. \quad (17)$$

In order to obtain a relationship between the filtered MODTRAN3 radiance and the nonfiltered CKD radiance, 83 cases were identified when clear sky conditions occurred near a 0000 or 1200 UTC balloon sounding launch from the nearby SLC-NWSFO. Cloudless sky conditions were determined using lidar backscatter profile measurements. The model downwelling clear-sky radiance at the surface is then calculated using both the FARS CKD model and the MODTRAN3 filtered and integrated results for each clear-sky sounding. A scatterplot of filtered to unfiltered model radiance yields a linear relationship with a correlation coefficient of 0.999. This relationship is used to correct the model downwelling radiance at the surface for the IR radiometer filter function. The FARS CKD model is approximately 56% faster than MODTRAN3 for calculations of a vertical profile of downwelling radiance under clear sky conditions, which greatly reduces the computation time when applying this retrieval to the FARS long-term dataset.

The above described method for adjusting model radiance to account for the radiometer filter function applies only to the model-derived downwelling radiance at the surface. It is also important to adjust the model radiance profile because an estimate of the radiance due to gases above and below the cloud is required for the calculation of the cloud radiance, which will be explained in section 3d. In this study, we correct the model radiance profile by using the gamma correction technique described in Smith et al. (1993), which iteratively adjusts the profile of atmospheric transmittance until the desired surface radiance is obtained (which, in our case, is a filtered radiance).

Comparisons have been performed between the FARS model and MODTRAN3 to exhibit the reliability of the CKD radiation code. The model-derived downwelling radiance, with the filter function and gamma correction included, agrees to 1.1% with MODTRAN3. In addition to the above comparison, Duffy (1996) provides extensive sensitivity studies and comparisons of the FARS CKD model with line-by-line calculations. The CKD model was found to be within 2% of FASCODE3 for both U.S. standard and midlatitude summer atmospheric profiles. Only in the subarctic winter case were errors larger (~3.6%).

4) MWR CORRECTION OF WATER VAPOR MIXING RATIOS

Precipitable water vapor W_{MWR} derived from MWR measurements is an important parameter that can be used to correct radiosonde derived mixing ratio r. The MWR can also be used to account for temporal changes in the water vapor between 12-h sounding times. This will improve the accuracy of model-derived radiances and ε. Water vapor mixing ratio is corrected by first taking a ratio of W_{MWR} to the total integrated water W_s derived from a radiosonde profile. The density $\rho_v(z)$ of moist air for each atmospheric layer is then adjusted according to

$$\rho_v^{\mathrm{new}}(z) = \frac{W_{\mathrm{MWR}}}{W_s}\rho_v(z). \quad (18)$$

The MWR adjusted mixing ratio is obtained by taking the ratio of $\rho_v^{\mathrm{new}}(z)$ to the density $\rho_d(z)$ of dry air.

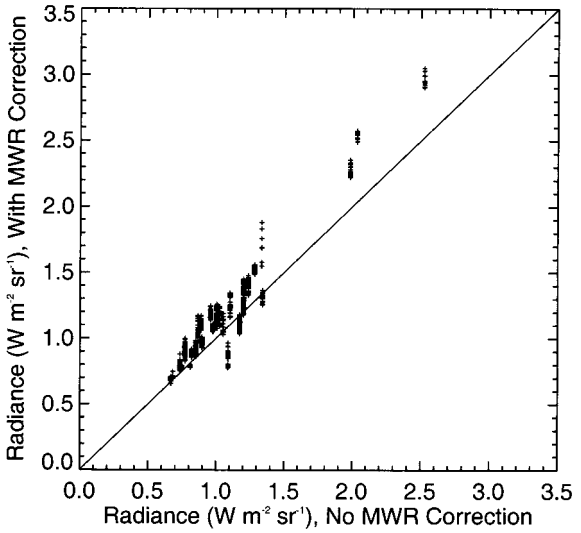

FIG. 5. Comparison of model-derived clear-sky downwelling radiances at the surface for uncorrected and MWR-corrected water vapor mixing ratios.

d. Calculation of cloud radiative properties

The primary cloud radiative properties derived in this retrieval are IR emittance ε and visible optical depth τ. Cloud emittance is obtained by combining the IR radiometer and lidar backscatter measurements with the FARS CKD radiative transfer model, as we now describe.

1) MEASURED CLOUD RADIANCE I_c AND CLOUD EMITTANCE ε

The measured IR radiance I_m is combined with the radiative transfer model described in section 3c to estimate the cloud radiance I_c. The equation used to estimate I_c is

$$I_c = \frac{I_m - I_{sr}T_{bc} - I_g}{T_{bc}}, \tag{19}$$

where

$$I_g = I_{ac}T_cT_{bc} + I_{ic}T_{bc} + I_{bc}. \tag{20}$$

The transmittance below the cloud T_{bc}, and the radiance due to the emission of atmospheric gases above, below, and in the cloud, I_{ac}, I_{bc}, and I_{ic}, respectively, are derived using the CKD model. The upwelling radiance that is reflected by the cloud downward into the radiometer FOV, which we call I_{sr}, is an important contributor to I_m (Platt 1973). The current retrieval uses a new parameterization of I_{sr} that is derived from radiative transfer simulations and microphysical considerations, as discussed below in section 3d(2).

The cloud IR absorption coefficient $\sigma_a(z)$ is related to $\beta_c(z)$ using the expression $\sigma_a(z) = \zeta\beta_c(z)$, where ζ is an unknown constant that we initially set to 0.01. The theoretical cloud radiance I_{ct} is then calculated using Eq. (6). The parameter ζ is varied until $I_{ct} \cong I_c$, and the final value of $\sigma_a(z)$ is used to estimate ε following Eq. (8). The ratio of the layer mean visible extinction and IR absorption coefficients, σ_c and σ_a, respectively, is defined as $\alpha = \sigma_c/\sigma_a$, and can be used to infer particle size (Mitchell and Platt 1998).

TABLE 2. Average single-scattering properties used in deriving I_{ST} and T_C, where g is the asymmetry factor, $1 - \tilde{\omega}$ is the coalbedo, and σ_e is the extinction coefficient. The size categories are determined by the generalized effective size D_{ge} (Fu 1996).

Size	g	$1 - \tilde{\omega}$	σ_e
Small ($D_{ge} < 30$ μm)	0.856	0.376	0.178
Medium ($30 \le D_{ge} \le 65$ μm)	0.920	0.407	0.244
Large ($D_{ge} > 65$ μm	0.960	0.440	0.710

2) UPWELLING RADIANCE REFLECTED BY CLOUDS I_{sr}

In past studies, I_{sr} was calculated using the assumption that cirrus ice crystals are shaped as ''equivalent'' ice spheres (Hall 1968) or long ice cylinders (Platt and Stephens 1980). In situ measurements in cirrus clouds have revealed that cirrus particles have a variety of shapes, such as hexagonal plates, columns, bullet rosettes, and aggregates (Heymsfield and Platt 1984; Sassen et al. 1994). Therefore, to properly compute the amount of radiance scattered into the FOV of the radiometer, one should use detailed ice crystal scattering properties. Single-scattering properties (at 10-μm wavelength) of 28 distinct ice crystal size distributions derived from various in situ measurements in cirrus clouds were obtained using a combination of Mie and finite-difference time domain calculations (Fu 1996; Fu et al. 1998). The scattering phase functions of ice crystals are subsequently modeled using the Henyey–Greenstein relation. The discrete ordinate model (Stamnes et al. 1988) for multiple scattering and the reciprocity principle (Stamnes and Swanson 1981) were used to estimate the reflectance $R(\theta)$ of the cloud at various scattering angles θ. The FARS CKD model estimates the upwelling radiance $I^{\uparrow}(z_b, \theta)$ incident at cloud base over the bandwidth of the IR radiometer. Integrating $R(\theta)I^{\uparrow}(z_b, \theta)$ over the downward hemisphere, we have

$$I_{sr} = \frac{1}{4\pi}\int_0^{80^\circ} I^{\uparrow}(z_b, \theta)R(\theta)\, d\theta. \tag{21}$$

Simulations of I_{sr} for all 28 different size distributions reveal a distinct relationship between I_{sr} and both IR optical depth τ_{IR} and ice crystal size (Fig. 4). Dividing ice crystal sizes into three groups labeled small, medium, and large (Table 2), we find that the amount of reflected radiance is generally higher for cirrus clouds with smaller particles. In fact, the magnitude of I_{sr} varies substantially with τ_{IR}, surface ground temperature, atmospheric transmittance, ice crystal size, and, to a lesser extent, on cloud height.

TABLE 3. Fractional uncertainties in measured and derived quantities used in the sensitivity analysis. The parameter T_b denotes the measured brightness temperature.

Measured quantities	F
Temperature (°C)	1.4×10^{-2}
Dewpoint (°C)	3.3×10^{-2}
IR radiometer ($T_b = 0$°C)	9.3×10^{-3}
IR radiometer ($T_b = -80$°C)	1.9×10^{-2}
Lidar range (m)	4.7×10^{-4}
Derived quantities	F
I_b	1.5×10^{-2}
I_c	1.7×10^{-1}
I_g	5.1×10^{-2}
T_{bc}	1.4×10^{-2}
z_b	4.7×10^{-3}
z_t	4.7×10^{-3}
$k/2\eta$	3.0×10^{-1}
k	3.3×10^{-1}
η	1.2×10^{-1}

TABLE 4. Results from the sensitivity analysis of ϵ and τ. The average change ($\Delta\epsilon$ and $\Delta\tau$) is calculated for each perturbation in measured and derived quantities.

Perturbed quantity	Amount changed	$\Delta\epsilon$ (%)	$\Delta\tau$ (%)
I_m	11.9%	33.4	0.0
T	2.0%	2.61	0.0
T_d	3.3%	2.19	0.0
z_b	+75 m	−0.572	−3.40
z_b	−75 m	0.165	−0.196
z_t	−75 m	−0.0273	−1.65
z_t	+150 m	0.438	1.74
T_s	20.0%	−3.63	0.0
k	32.5%	0.0	−24.5
$k/2\eta$	30.2%	−1.56	−33.2
η	12.0%	0.232	9.30
I_b	1.5%	−1.47	0.0
I_c	17.3%	16.0	0.0
I_g	5.1%	−8.99	0.0
T_{bc}	1.44%	−1.59	0.0

In the present LIRAD retrieval, I_{sr} is calculated for each cloud system using a ''best guess'' for the ice crystal size distribution based on the observed cloud type as revealed by lidar depolarization measurements and field notes. For example, an estimate of the particle size can be determined by the appearance of optical phenomena in cirrus clouds. Sassen (1997) explains how cirrus cloud layers that display a corona or aureole have relatively small particles (~10–30 μm), whereas cirrus clouds that display halos and arcs generally contain large (at least 100 μm in maximum dimension) oriented hexagonal plate crystals (Sassen 1980). Based on criteria such as these, as well as cloud-base temperature, the size distribution is chosen for each cloud during periods where the cloud appears to be homogeneous. Once the size distribution is specified, the single-scattering properties used to determine I_{sr} are chosen based on the average values indicated in Table 2.

4. Sensitivity analysis

a. Uncertainties in derived radiative properties

In order to assess the accuracy of the retrieval of radiative properties using the FARS–LIRAD algorithm, a detailed sensitivity analysis has been performed. Fractional uncertainties F in measured quantities are estimated using manufacturer supplied instrument specifications and calibration uncertainties (Table 3). For example, the fractional uncertainty in the temperature T and dewpoint T_d are determined by the accuracy of the radiosonde sensors. The measured IR radiance has a combined F of 0.119, which includes instrument sensitivity and calibration uncertainty. Errors associated with the measured quantities are propagated to derived quantities, such as ε and τ, through the retrieval algorithm. The total uncertainty in the estimated cloud radiance is 0.173, which is a result of uncertainties in the measured radiance, cloud boundaries, the CKD model radiance, and other components of Eqs. (19) and (20). Uncertainties in the quantities k and η are also displayed in Table 3.

A variety of sensitivity tests were performed on a 1-yr period of lidar and IR radiometer data, amounting to 136 different observation periods with approximately 95 h of measurements. The uncertainties listed in Table 3 were applied to these measurements to estimate the errors in τ and ε. Our methodology was to first create a reference run for the 1-yr period of estimated cloud IR emittance and visible optical depth using the retrieval algorithm described in this paper. In each subsequent run, one quantity was perturbed by the amount listed in Table 4. For example, an 11.9% change in the measured radiance results in a 33.4% change in ε, which is the largest source of error. It is notable that overestimating the cloud base by 75 m results in an average change in τ and ε of only 3.4% and 0.57%, respectively. Similarly, overestimating z_t by 150 m causes an average $\Delta\tau = 1.74\%$ and $\Delta\varepsilon = 0.438\%$.

As displayed in Table 4, the largest uncertainty associated with calculating τ is the determination of k, otherwise, there is negligible change. Further calculations indicate that the average uncertainty in τ is approximately 24.5% and is independent of midcloud temperature and the magnitude of τ. This is mainly due to the physical and mathematical nature of the method used to derive k and τ. Although the overall uncertainty is high, the accuracy required for estimations of longwave fluxes is low. For example, Brown et al. (1995) studied the accuracy of τ required for calculations of outgoing longwave radiation (OLR) and model-derived surface fluxes for climate studies, and report that for OLR to be calculated within ± 10 W m^{-2}, the required accuracy of τ must be within +100% and −50% of the actual value. This value is sufficient for optical depths as low as 0.07 in midlatitude locations. The accuracy required for estimating downward fluxes within ± 5 W m^{-2} is even less stringent according to Brown et al. (1995).

TABLE 5. Average change in ϵ in percent due to perturbations in radiances and $k/2\eta$ as listed in Table 3. Averages are listed for three temperature and ϵ divisions.

	I_c	I_m	$k/2\eta$
$T_m \leq -60$°C	16.9	33.8	−1.07
-60°C $< T_m \leq -40$°C	16.1	39.2	−1.39
$T_m > -40$°C	16.0	27.9	−1.73
$\epsilon \leq 0.3$	16.3	44.2	−0.579
$0.3 < \epsilon < 0.7$	15.5	16.8	−3.15
$\epsilon \geq 0.7$	16.2	13.6	−2.18

Therefore, the average uncertainty in τ derived using the FARS–LIRAD method is well within the accepted accuracies needed for climate applications.

Changes in ε as a function of midcloud temperature T_m, determined from a radiosonde profile, are displayed in Table 5. There does not appear to be a large effect of midcloud temperature on the uncertainty in ε; however, errors in ε are most sensitive to perturbations in I_m for T_m between $-40°$ and -60°C. Also listed in Table 5 are the variations in uncertainty of ε for different ε intervals. The lowest ε interval has the largest uncertainty due to changes in I_m. This is primarily caused by the small IR emission of cold, thin clouds that often radiate just above the cloudless background signal measured by the IR radiometer. Note that although changes in $k/2\eta$ do not affect ε for different temperatures, there is a higher variation in ε for $\varepsilon > 0.3$ when perturbing $k/2\eta$.

b. *Improvements using MWR-corrected water vapor mixing ratios*

As described in section 3c, radiosonde-derived mixing ratio r can be corrected for temporal variations in column water vapor using MWR measurements. Adjusting r using the MWR also helps correct the apparent dry bias in radiosonde water vapor measurements mentioned in section 2. To assess the improvement of MWR corrections to derived radiances, downwelling IR radiance at the surface has been estimated using both radiosonde-derived and MWR-corrected mixing ratios. Observations of clear-sky radiance were identified using lidar backscatter profiles between October 1998 and June 1999. Downwelling clear-sky radiance at the surface is then calculated using both corrected and uncorrected mixing ratios at the radiosonde launch times (Fig. 5). Model radiances with the MWR correction are on average 7.8% higher than without the correction. Note that Fig. 5 also displays the tendency for the difference between corrected and uncorrected radiances to increase with increasing water vapor amounts. FARS is located in an arid climate and during cirrus observations W_{MWR} is usually small, allowing for the retrieval of ε from low optical depth clouds. However, in moist climates, such as the Tropics, correcting for the dry bias in the radiosonde dewpoint measurement will be more important, particularly when deriving ε for small τ cases.

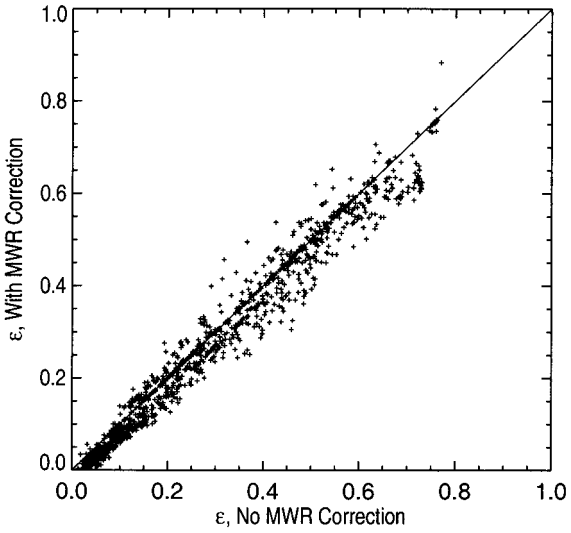

FIG. 6. Comparison of cloud emittance estimated using radiosonde-derived and MWR-corrected water vapor mixing ratios.

The correlation between ε estimated using radiosonde-derived and MWR-corrected mixing ratios is illustrated in Fig. 6. Cloud emittance is calculated for the same time periods as in Fig. 5, but for all cirrus observations rather than just clear sky observations. There is a noticeable bias toward higher ε when no MWR correction is used. The MWR corrected ε is on average 20% lower than the uncorrected ε. Although the MWR clearly provides an improvement to model-derived radiances, the overall average uncertainty in retrievals of radiative properties without MWR measurements is minimized when a large number of observations are analyzed. This result may differ for regions where column water vapor amounts are higher and vary significantly over time.

As mentioned previously, radiosonde data from the SLC-NWSFO are available only twice daily and the MWR can be used to adjust for the variability of water vapor between 12-h sounding data (Fig. 7). In Fig. 7, there is approximately a 0.4-cm change in the precipi-

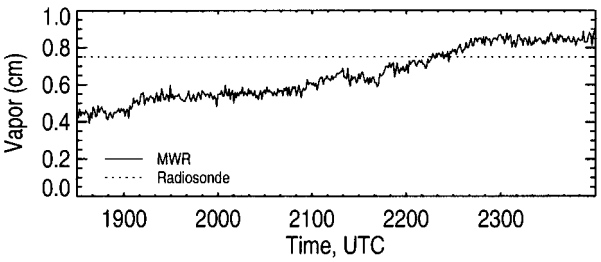

FIG. 7. Column water vapor measured by the MWR and derived from radiosonde data. Note that the constant W from radiosonde data represents the case where the column water vapor is assumed to be constant between 12-h soundings.

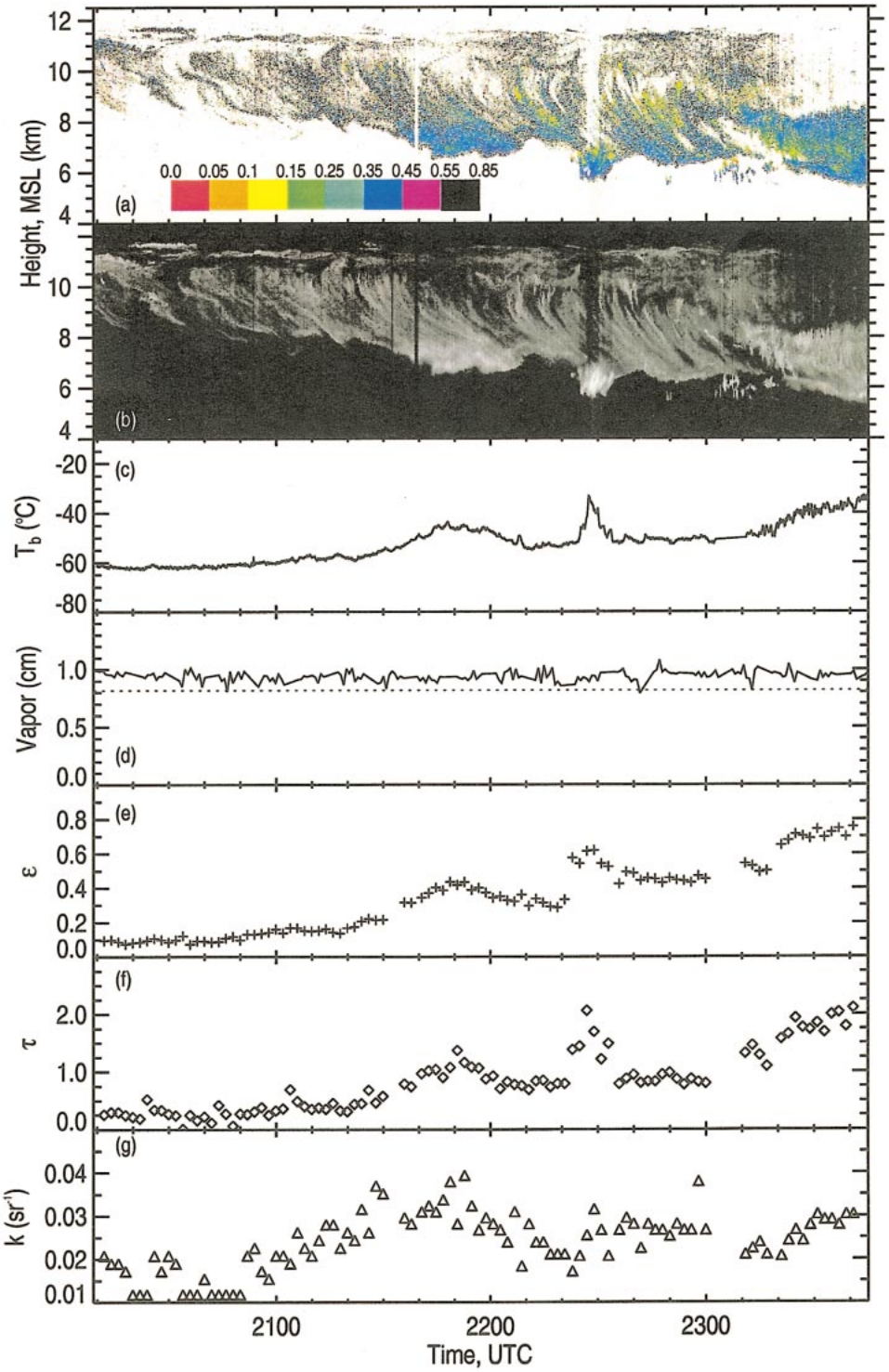

FIG. 8. Case study of a synoptic generated cirrostratus measured at FARS on 6 Jan 1999 (a) Time–height displays of δ and (b) lidar relative returned energy based on a logarithmic grayscale, (c) brightness temperature measured by the IR radiometer, (d) MWR and radiosonde measurements of W, (e) ε, (f) τ, and (g) k.

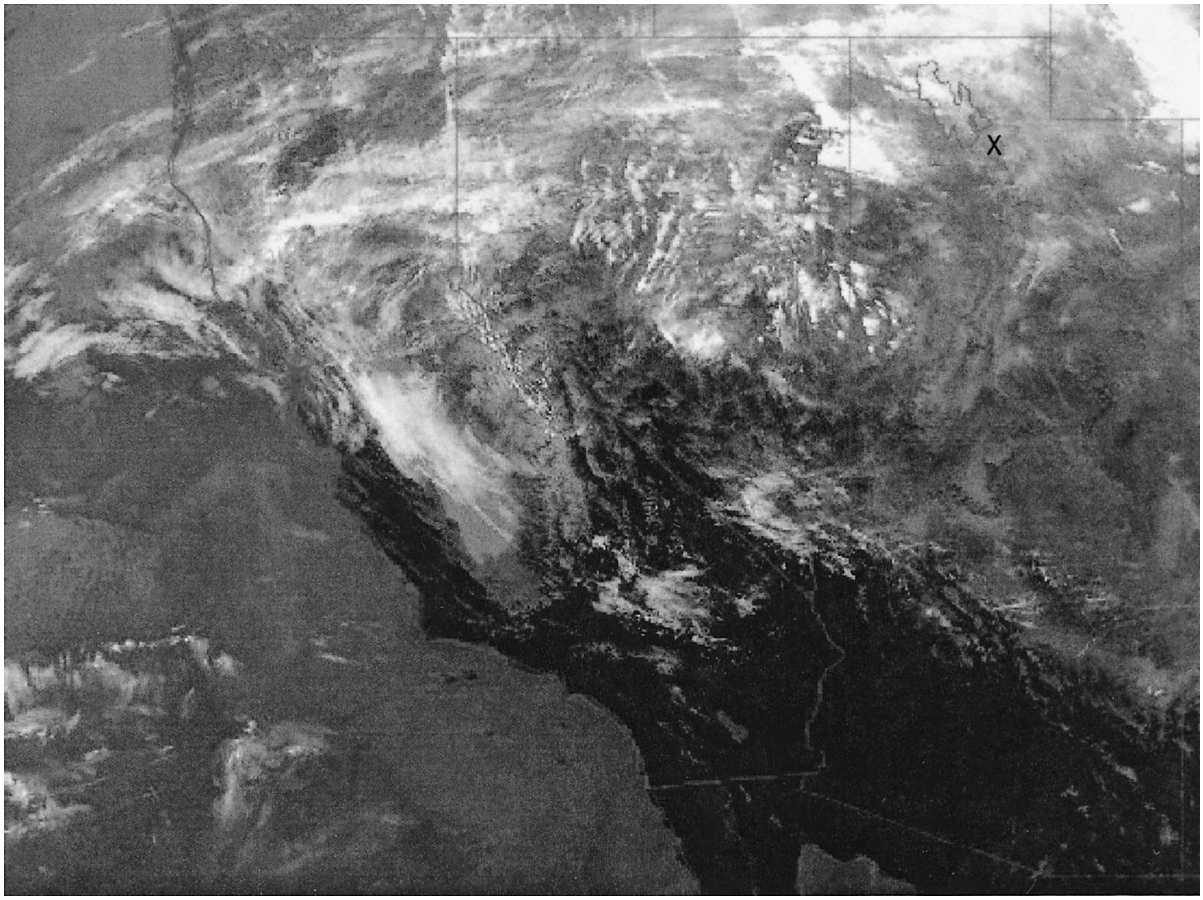

FIG. 9. NOAA polar orbiter *NOAA-14* image from the 10-μm channel taken at 2223 UTC 6 Jan 1999, displayed for the southwestern United States. FARS is located to the southeast of the Great Salt Lake, denoted with an ''X.'' There are several contrails visible in the satellite image.

table water vapor over the 5.5-h time period. The sounding is slightly lower than W_{MWR} at the 0000 UTC launch time at the end of the period, as expected. During this time period, ε is up to 30% lower when using W_{MWR} due to the overestimation of the downwelling radiance when the correction is not used. This example shows how 12-h soundings are not always representative of the atmospheric conditions at the time of LIRAD measurements, and how the MWR can be used to reduce the uncertainty in the model radiances and ε.

5. Case study

The following case study has been chosen to demonstrate the abilities of the FARS LIRAD algorithm to derive radiative and backscattering properties of cirrus clouds. Depolarization ratio and backscattered energy measured by the ruby lidar on 6 January 1999 at FARS are illustrated in Figs. 8a and 8b. The general synoptic conditions consist of a jet stream located to the northwest of Salt Lake City with local thin cirrostratus and fibratus, followed by denser bands. Figures 9 and 10 depict the Advanced Very High Resolution Radiometer satellite imagery and radiosonde data that correspond with the cirrus observations. Since the wind barbs in Fig. 10 indicate 28.1 m s^{-1} westerly winds at cirrus levels near 10 km, the cirrus to the east of FARS in Fig. 9 coincides with the lidar time-height display. According to the FARS lidar operator, several contrails were visible in the sky.

As indicated by Fig. 8, the cirrus was visibly thin until 2100 UTC, when the IR radiometer brightness temperature (Fig. 8c) began a slow increasing trend. (Note the small gap in the IR radiometer measurements between 2300 and 2310 UTC.) At 2230, when a weak 22° halo and broad sundogs became visible above FARS, the lidar signal appears to become attenuated. However, the region of strong backscattering near cloud base at this time led to a lowering of the gains of the detector channels, such that the weaker signals aloft were possibly no longer detected. Eventually, at 2320, the cloud becomes opaque and cellular as large cirrocumulus cells drift overhead. The atmospheric optical phenomena visible earlier ceased about this time as well.

The column water vapor W measured by the MWR and derived from the 0000 UTC 7 January 1999 radio-

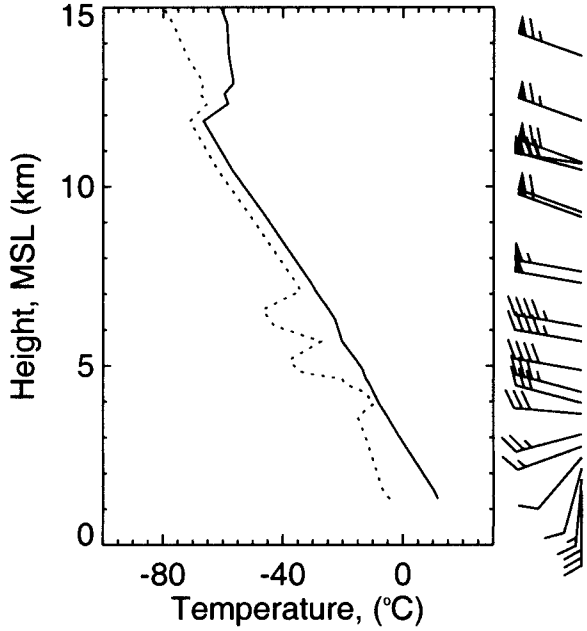

FIG. 10. SLC-NWSFO sounding for 0000 UTC 7 Jan 1999. Wind barbs are given in 2.5, 5.1, and 25.6 m s^{-1} intervals.

sonde data is displayed in Fig. 8d. The MWR values are generally constant during the nearly 4-h time period. The sounding derived W is only slightly less than the MWR, which is typical when comparing the two measurements. In this case, an average discrepancy of 11% in W results in an average difference of 10% in the model clear sky radiance at the surface and a 14% difference in the derived ε.

Estimates of ε and τ using the FARS–LIRAD algorithm are depicted in Figs. 8e and 8f. During the first hour of the observing period, the IR radiometer brightness temperature is only slightly above the background signal due to emission of atmospheric gases, which is also indicated in the low values of $\varepsilon \sim 0.07$ to 0.1 and τ ranging from 0.05 to 0.3. During this time period, k is quite small (Fig. 8g), which may indicate the presence of simple crystals, such as hollow columns that have been shown to have small backscatter phase functions (Takano and Liou 1995). Grund and Eloranta (1990) have also measured values of k as low as 0.01 sr^{-1} in a cirrus cloud with $\tau < 0.1$ using a different technique. As denser cirrus cloud bands passed overhead, both ε and τ increased. Toward the end of the observation period, τ eventually approached the upper limit ($\tau \sim 3.0$) in lidar measurement capabilities of optical depth before complete attenuation. There are weak signals to cloud top between 2320 and 2345, indicating that the lidar signal is not attenuated and that τ of 2.5 is associated with the full depth of the cloud. During this period ε also reached approximately 0.8. The parameter k tends to be higher between 2150 and 2300 when the 22° halo and weak upper tangent arc were visible. The linear depolarization ratio δ in Fig. 8a appears to have patches

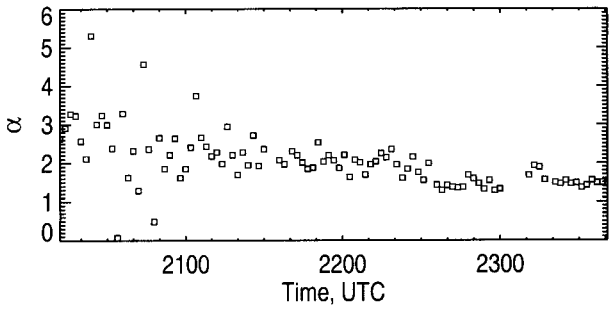

FIG. 11. Extinction-to-absorption ratio α vs time for the case study displayed in Fig. 9.

of relatively low values at this time. Low δ values are an indication of the presence of horizontally oriented hexagonal plate crystals (Sassen and Benson 2001), which will have higher $\mathcal{P}(\pi)$ and therefore higher k.

The time series of α (Fig. 11) reveals slightly higher ratios in the first hour of observations, which can be an indication of the presence of smaller ice crystals in cirrus clouds. The large amount of scatter in α before 2100 is likely due to the uncertainty associated with estimating small ε. The thin cirrus cloud at this time has low ε and therefore the uncertainty (as discussed in section 4) in ε and σ_a is higher than later when ε and τ increase. As the cirrus becomes denser and the size of ice crystals increases, α oscillates around 2, which is in the geometric optics limit.

6. Conclusions

This paper describes extensions to the LIRAD retrieval algorithm originally developed by Platt (1973). The algorithm presented here includes several improvements, including the use of a detailed radiative transfer code that allows for more accurate estimation of the upwelling radiance reflected by the cloud. The current approach also uses a technique for estimating the backscatter-to-extinction ratio for each lidar profile, rather than a single value for the entire cloud system. This change allows for variations in the microphysical properties of cirrus as the cloud evolves, which will affect the derived k. This algorithm was designed to analyze the FARS high-cloud dataset (Sassen et al. 2001b; Sassen and Campbell 2001; Sassen and Benson 2001; Sassen and Comstock 2001) collected during our support of the extended time observations satellite validation effort of Project FIRE. However, this algorithm can be used by any backscatter lidar and IR radiometer combination intended to obtain τ and ε with sufficient accuracy for climate studies.

The sensitivity analysis details the uncertainties associated with both measured and derived quantities, identifying many sources of error that are a result of the assumptions in the LIRAD method. In particular, for cases with small ε, when the measured brightness temperatures are only slightly higher than the background, uncertainty in the radiative transfer model leads

to increased uncertainty in the derived ε. This is mainly due to uncertainties in the estimation of the absorption coefficients for the water vapor continuum. We also show the utility of employing a microwave radiometer to obtain improved column water vapor amounts.

Results presented for a developing synoptic cirrostratus system reveal how the present LIRAD algorithm can be used to retrieve reasonable values of ε and τ, and also produce some information on the cirrus microphysics by combining measurements of δ, k, and α. This research illustrates the capabilities of ground-based observations for the verification of cloud properties derived from satellite radiance measurements, a major goal of our participation in Project FIRE.

The primary purpose for developing this algorithm was for the analysis of long-term observations of high clouds at FARS (Sassen and Comstock 2001). This dataset represents a climatologically representative sample of midlatitude cirrus clouds, from which we have developed a parameterization of their radiative properties (Sassen et al. 2001b) relating midcloud temperature and cloud thickness with IR absorption coefficient, and importantly, cloud visible optical depth and infrared layer emittance. These improvements to the LIRAD method and the development of radiative parameterizations from the extensive FARS dataset will contribute to better treatment of cirrus clouds in weather and climate models, and satellite cloud research.

Acknowledgments. This research has been funded primarily by NSF Grant ATM-9528287. The authors would like to thank Dr. Q. Fu for providing single-scattering properties and useful comments during the development of this algorithm. We also thank Dr. Z. Wang for useful discussions pertaining to this work and L. Wang for preparing the satellite imagery.

APPENDIX

List of Symbols

T_d	Dewpoint temperature
T	Atmospheric temperature
p	Atmospheric pressure
$\rho\,(\rho_v)$	Density of dry (moist) air
r	Water vapor mixing ratio
W_s,	W_{MWR} column-integrated water vapor derived from radiosonde and microwave radiometer measurements, respectively
z_b,	z_t cloud-base and cloud-top heights
z_{tos}	Maximum height measured by the lidar
k	Backscatter-to-extinction ratio
α	Extinction-to-absorption ratio
η	Forward multiple-scattering correction factor
$P(R)$	Lidar backscattered power as a function of range
δ	Linear depolarization ratio
σ_c	Volume extinction coefficient at 0.694 μm
σ_a	Volume absorption coefficient at 9.25–12.0 μm
β,	β' volume backscatter coefficient for single and mulitple backscattered photons, respectively
β_m,	β_c molecular and cloud backscatter coefficients, respectively
$T_{\bar{v}}$	Transmittance of atmospheric layer
K	Absorption coefficient used in the correlated K distribution model
$g(K)$	Cumulative probability as a function of absorption coefficient
$\mathcal{P}(\Theta)$	Phase function as a function of scattering angle
$R(\theta)$	Reflectance as a function of angle
τ	Visible optical depth at 0.694 μm
τ_{IR}	Optical depth at 10.0 μm
ε	IR emittance
$I_{\bar{v}}^{\uparrow,\downarrow}$	Upwelling and downwelling radiance at 9.25–12.0 μm
I_b	Blackbody radiance
I_c	Radiance emitted by cloud ice particles only, derived from measured IR radiance
I_m	Radiance measured by IR radiometer
I_{sr}	Upwelling radiance reflected by cloud into radiometer FOV
I_{ac}	Downwelling radiance due to emission by atmospheric gases above the cloud
I_{ic}	Downwelling radiance due to emission by atmospheric gases in the cloud
I_{bc}	Downwelling radiance due to emission by atmospheric gases below the cloud
I_{ct}	Theoretical cloud radiance
I_{sc}	Emitted radiance that is scattered in and out of the radiometer FOV
I_{sky}	Emission due to atmospheric gases used in original LIRAD method
T_{bc}	Atmospheric transmittance between cloud base and surface
T_c	Transmittance of layer between cloud base and top
T_m	Midcloud temperature
D_{ge}	Generalized effective size of ice crystals as defined in Fu (1996)
g	Asymmetry factor
$(1 - \tilde{\omega})$	Coalbedo

REFERENCES

Barnett, J. M., 2000: Remote sensing of midlatitude cirrus radiative properties: A seven-year climatology. Ph.D. dissertation, University of Utah, 220 pp.

Berk, A., L. S. Bernstein, and D. C. Robertson, 1989: MODTRAN: A moderate resolution model for LOWTRAN7. Tech. Rep. GL-TR-89-0122, 38 pp.

Brown, P. R. A., A. J. Illingworth, A. J. Heymsfield, G. M. McFarquhar, K. A. Browning, and M. Gosset, 1995: The role of spaceborne millimeter-wave radar in the global monitoring of ice cloud. *J. Appl. Meteor.*, **34,** 2346–2366.

Clough, S. A., F. X. Kneizys, E. Shettle, and G. Anderson, 1986: Atmospheric radiance and transmittance: FASCOD2. Preprints, *Sixth Conf. on Atmospheric Radiation,* Williamsburg VA, Amer. Meteor. Soc., 141–144.

——, ——, and R. W. Davies. 1989: Line shape and the water vapor continuum. *Atmos. Res.*, **23,** 229–241.
Cox, S. K., D. S. McDougal, D. A. Randall, and R. A. Schiffer, 1987: FIRE—The First ISCCP Regional Experiment. *Bull. Amer. Meteor, Soc.*, **68,** 114–118.
Duffy, K. J., 1996: A radiative transfer model to analyze radiometer data in the atmospheric window. M.S. thesis, Dept. of Meteorology, University of Utah, 94 pp.
Eloranta, E. W., 1998: Practical model for the calculation of multiply scattered lidar returns. *Appl. Opt.*, **37,** 2464–2472.
Fernald, F. G., B. M. Herman, and J. A. Reagan, 1972: Determination of aerosol height distributions by lidar. *J. Appl. Meteor.*, **11,** 482–489.
Fu, Q., 1996: An accurate parameterization of the solar radiative properties of cirrus clouds for climate models. *J. Climate*, **9,** 2058–2082.
——, and K. N. Liou, 1992: On the correlated *k*-distribution method for radiative transfer in nonhomogeneous atmospheres. *J. Atmos. Sci.*, **49,** 2139–2156.
——, Y. Ping, and W. B. Sun, 1998: An accurate parameterization of the infrared radiative properties of cirrus clouds for climate models. *J. Climate*, **11,** 2223–2237.
Grund, C. J., and E. W. Eloranta, 1990: The 27–28 October 1986 FIRE IFO cirrus case study: Cloud optical properties determined by High Spectral Resolution Lidar. *Mon. Wea. Rev.*, **118,** 2344–2355.
Hall, F. F., 1968: A physical model of cirrus 8–13 μ infrared radiance. *Appl. Opt.*, **7,** 2264–2269.
Heymsfield, A. J., and C. M. R. Platt, 1984: A parameterization of the particle size spectrum of ice clouds in terms of the ambient temperature and the ice water content. *J. Atmos. Sci.*, **41,** 846–854.
Kinne, S., T. P. Ackerman, A. J. Heymsfield, F. P. J. Valero, K. Sassen, and J. D. Spinhirne, 1992: Cirrus microphysics and radiative transfer: Cloud field study on 28 October 1986. *Mon. Wea. Rev.*, **120,** 661–684.
Lacis, A. A., and V. Oinas, 1991: A description of the correlated k distribution method for modeling nongray gaseous absorption, thermal emission, and multiple scattering in vertically inhomogeneous atmospheres. *J. Geophys. Res.*, **96,** 9027–9063.
Liou, K. N., 1986: Influence of cirrus clouds on weather and climate processes: A global perspective. *Mon. Wea. Rev.*, **114,** 1168–1199.
Macke, A., J. Mueller, and E. Raschke, 1996: Single scattering properties of atmospheric ice crystals. *J. Atmos. Sci.*, **53,** 2813–2825.
Matrosov, S. Y., B. W. Orr, R. A. Kropfli, and J. B. Snider, 1994: Retrieval of vertical profiles of cirrus cloud microphysical parameters from Doppler radar and infrared radiometer measurements. *J. Appl. Meteor.*, **33,** 617–626.
Mitchell, D. L., and C. M. R. Platt, 1998: Microphysical interpretation of LIRAD extinction/ absorption ratios using a microphysics-radiation scheme. *Proc. Eighth Atmospheric Radiation Measurement (ARM) Science Team Meetings*, Tucson, AZ, Department of Energy DOE/ER-0738, 495–498.
Nicolas, F., L. R. Bissonnette, and P. H. Flamant, 1997: Lidar effective multiple-scattering coefficients in cirrus clouds. *Appl. Opt.*, **36,** 3458–3468.
Ou, S. C., K. N. Liou, W. M. Gooch, and Y. Takano, 1993: Remote sensing of cirrus cloud parameters using advanced very-high-resolution radiometer 3.7 and 10.9 μm channels. *Appl. Opt.*, **32,** 2171–2180.
Platt, C. M. R., 1973: Lidar and radiometric observations of cirrus clouds. *J. Atmos. Sci.*, **30,** 1191–1204.
——, 1978: Lidar backscatter from horizontal ice crystal plates. *J. Appl. Meteor.*, **17,** 482–488.
——, 1981: Remote sounding of high clouds. Part III: Monte Carlo calculations of multiple-scattered lidar returns. *J. Atmos. Sci.*, **38,** 156–167.
——, and G. L. Stephens, 1980: Interpretation of remotely sensed high cloud emittances. *J. Atmos. Sci.*, **37,** 2314–2322.
——, and A. C. Dilley, 1981: Remote sounding of high clouds. Part IV: Observed temperature variations in cirrus optical properties. *J. Atmos. Sci.*, **38,** 1069–1082.
——, S. A. Young, P. J. Manson, G. R. Patterson, S. C. Marsden, and R. T. Austin, 1998: The optical properties of equatorial cirrus from observations in the ARM pilot radiation observation experiment. *J. Atmos. Sci.*, **55,** 1977–1996.
Roberts, E. R., J. E. A. Selby, and L. M. Biberman, 1976: Infrared continuum absorption by atmospheric water vapor in the 8–12 μm window. *Appl. Opt.*, **15,** 2085–2090.
Sassen, K., 1978: Backscattering cross sections for hydrometeors: Measurements at 6328 Angstroms. *Appl. Opt.*, **17,** 804–806.
——, 1980: Remote sensing of planar ice crystal fall attitudes. *J. Meteor. Soc. Japan*, **58,** 422–429.
——, 1991: The polarization lidar technique for cloud research: A review and current assessment. *Bull. Amer. Meteor. Soc.*, **72,** 1848–1866.
——, 1997: Contrail-cirrus and their potential for regional climate change. *Bull. Amer. Meteor. Soc.*, **78,** 1885–1903.
——, 2001: Cirrus clouds. A modern perspective. *Cirrus*. D. Lynch et al., Eds., Oxford University Press, 11–40.
——, and B. S. Cho, 1992: Subvisual-thin cirrus lidar dataset for satellite verification and climatological research. *J. Appl. Meteor.*, **31,** 1275–1285.
——, and H. Zhao, 1995: Lidar multiple scattering in water droplet clouds: Toward an improved treatment. *Opt. Rev.*, **2,** 394–400.
——, and S. Benson, 2001: A midlatitude cirrus cloud climatology from the Facility for Atmospheric Remote Sensing. Part II: Microphysical properties derived from lidar depolarization. *J. Atmos. Sci.*, **58,** 2103–2112.
——, and J. R. Campbell, 2001: A midlatitude cirrus cloud climatology from the Facility for Atmospheric Remote Sensing. Part I: Macrophysical and synoptic properties. *J. Atmos. Sci.*, **58,** 481–496.
——, and J. M. Comstock, 2001: A midlatitude cirrus cloud climatology from the Facility for Atmospheric Remote Sensing. Part III: Radiative properties. *J. Atmos. Sci.*, **58,** 2113–2127.
——, N. C. Knight, Y. Takano, and A. J. Heymsfield, 1994: Effects of ice-crystal structure on halo formation: Cirrus cloud experimental and ray-tracing modeling studies. *Appl. Opt.*, **33,** 4590–4601.
——, J. M. Comstock, Z. Wang, and G. G. Mace, 2001a: Cloud and aerosol research capabilities at FARS: The Facility for Atmospheric Remote Sensing. *Bull. Amer. Meteor. Soc.*, **82,** 1119–1138.
——, ——, and Z. Wang, 2001b: Parameterization of the radiative properties of midlatitude high and middle level clouds. *Geophys. Res. Lett.*, **28,** 729–732.
Smith, W. L., X. L. Ma, S. A. Ackerman, H. E. Revercomb, and R. O. Knuteson, 1993: Remote sensing cloud properties from high spectral resolution infrared observations. *J. Atmos. Sci.*, **50,** 1708–1720.
Stamnes, K., and R. A. Swanson, 1981: New look at the discrete ordinate method for radiative transfer calculations in anisotropically scattering atmospheres. *J. Atmos. Sci.*, **38,** 387–399.
——, S. C. Tsay, W. Wiscombe, and K. Jayaweera, 1988: Numerically stable algorithm for discrete-ordinate-method radiative transfer in multiple scattering and emitting layered media. *Appl. Opt.*, **27,** 2502–2509.
Takano, Y., and K. N. Liou, 1995: Radiative transfer in cirrus clouds. Part III: Light scattering by irregular ice crystals. *J. Atmos. Sci.*, **52,** 818–837.
Turner, D. D., T. R. Shippert, P. D. Brown, S. A. Clough, R. O. Knuteson, H. E. Revercomb, and W. L. Smith, 1998: Long-term analyses of observed and line-by-line calculations of longwave surface spectral radiance and the effect of scaling the water vapor profile. *Proc. Eighth Atmospheric Radiation Measurement (ARM) Science Team Meetings*, Tucson, AZ, Department of Energy DOE/ER-0738, 773–776.
——, W. F. Feltz, and R. A. Ferrare, 2000: Continuous water vapor profiles from operational ground-based active and passive remote sensors. *Bull. Amer. Meteor. Soc.*, **81,** 1301–1318.
Young, S. A., 1995: Analysis of lidar backscatter profiles in optically thin clouds. *Appl. Opt.*, **34,** 7019–7031.